**Key Points:**
- A new measure of global subseasonal variability provides scale and dynamics dependent variability estimates
- An increase in variability in recent years for about 2% relative to 1981 to 2010 is found in ERA-Interim data
- The increase is larger in variability associated with inertio-gravity modes than with Rossby modes

**Correspondence to:**
N. Žagar,
nedjeljka.zagar@fmf.uni-lj.si

# Estimating Subseasonal Variability and Trends in Global Atmosphere Using Reanalysis Data

**N. Žagar[1]** ![ID], **D. Jelić[1,2], M. J. Alexander[3]** ![ID]**, and E. Manzini[4]** ![ID]

[1]Faculty of Mathematics and Physics, University of Ljubljana, Ljubljana, Slovenia, [2]Faculty of Science, University of Zagreb, Zagreb, Croatia, [3]NWRA/Colorado Research Associates, Boulder, CO, USA, [4]Max-Planck-Institut fur Meteorologie, Hamburg, Germany

**Abstract** A new measure of subseasonal variability is introduced that provides a scale-dependent estimation of vertically and meridionally integrated atmospheric variability in terms of the normal modes of linearized primitive equations. Applied to the ERA-Interim data, the new measure shows that subseasonal variability decreases for larger zonal wave numbers. Most of variability is due to balanced (Rossby mode) dynamics but the portion associated with the inertio-gravity (IG) modes increases as the scale reduces. Time series of globally integrated variability anomalies in ERA-Interim show an increase in variability after year 2000. In recent years the anomalies have been about 2% above the 1981–2010 average. The relative increase in variability projecting on the IG modes is larger and more persistent than for the Rossby modes. Although the IG part is a small component of the subseasonal variability, it is an important effect likely reflecting the observed increase in the tropical precipitation variability.

**Plain Language Summary** The multiaspect nature of atmospheric variability has traditionally been approached by analyzing selected spatiotemporal components of circulation variability. For example, estimating trends in extreme events often rely on surface temperature and precipitation data that can be validated with long observation records. Trends in circulation need to be analyzed using global gridded three-dimensional data which are provided by reanalyses. This article provides the first quantification of global subseasonal variability using reanalysis data. A new measure, named subseasonal variability integral, spatially integrates variability in surface pressure and variability in winds and geopotential height (i.e., temperature) on levels in the troposphere and stratosphere. The subseasonal variability integral is applied to the ERA-Interim reanalyses. Results show that estimated subseasonal variability has on average increased for about 2% in recent years relative to 1981–2010. A larger and more persistent increase is found in the inertio-gravity modes which are to a large extent associated with tropical unbalanced circulation. This likely reflects previously reported increase in latent heat in ERA-Interim and the observed increase in precipitation variability.

## 1. Introduction

Recent years have seen a number of extreme events on subseasonal time scales (Academies National, 2016). Estimates of the trends in extreme events often rely on 2-m temperature and precipitation data in reanalyses and climate model simulations that can be validated with long observation records. Trends in circulation are more difficult to validate (Shepherd, 2014) and the results may be inconclusive (Knutti & Sedlacek, 2013). Simmons et al. (2014, 2017) estimated low-frequency variability and trends in temperature data in interim reanalysis data of the European Centre for Medium-Range Weather Forecasts (ECMWF; ERA-Interim, Dee et al., 2011) and compared it with observations and other reanalysis products. They showed a good agreement between ERA-Interim and temperature measurements at surface, by radiosondes and by adjusted satellite brightness temperatures. Temperature variations in the tropical upper troposphere were shown to correlate well with those at the surface, but their amplitude is more than doubled, in agreement with modeling (Simmons et al., 2014).

Another metric of global change evaluated in Simmons et al. (2017) was monthly anomalies in atmospheric energy relative to 1981–2010. The energy metric reflects not only surface temperature but also the upper-air temperature and moisture content. This is particularly suitable for the Tropics, where the thermal signal has

greater vertical penetration and latent energy is a larger factor. Simmons et al. (2017) showed that total energy and its dominant thermal and latent energy components in ERA-Interim during the period since 1980 have varied in concert with surface temperature anomalies although with different amplitudes depending on season and low-frequency variability.

Here we ask the following question: how the reported changes in global temperature and energy influence global subseasonal variability? As today, there is no a standard method which would quantify the amount of global subseasonal variability. Its multiaspect nature is approached by analyzing selected spatiotemporal components known as *preferred* variability patterns (Cubasch et al., 2013). Precipitation variability has been investigated by analyzing frequency of events with certain amplitudes in different regions. White et al. (2017) showed that the number of precipitation events lasting 1–5 days in the 40°S–40°N spatial average significantly increased after 2000 in both ERA-Interim and Tropical Rainfall Measuring Mission observations. Their results are consistent with an independent estimate of increased frequency of mesoscale organized deep convection by Tan et al. (2015). Changes in precipitation and convection imply changes in latent heat release, a fundamental source of dynamical perturbations, especially in the tropics where the equatorial planetary waves and inertia gravity waves are large contributors to atmospheric subseasonal variability (e.g., Alexander et al., 2017; Grise & Thompson, 2012; Kasahara, 1984). As the observed trends in precipitation variability are in accord with the trend in atmospheric energy components reported in Simmons et al. (2017), it is natural to investigate whether changes in global dynamic variability can be detected in the reanalysis data.

The presented novel method provides scale-dependent estimates of subseasonal variability in horizontal winds and in a geopotential height variable and is particularly suited for reanalyses and climate models. The new measure is applied to the ERA-Interim data used by the above mentioned studies. Results indicate an increase in the global subseasonal variability in ERA-Interim reanalyses after 2000 relative to 1981–2010 that can be coupled to the observed precipitation changes, and to the latent energy and surface temperature changes in the reanalysis, but that also calls for a comparison with other reanalysis data sets.

## 2. Data and Method

Subseasonal variability is defined as the standard deviation of daily values from the seasonal mean. For example, for zonal wind at location $(\lambda, \varphi, p)$, subseasonal variability denoted $S_u$ is the square root of subseasonal variance $S_u^2$ given by

$$S_u^2 = \frac{1}{N-1} \sum_{t=1}^{N} \left( u(t) - \overline{u} \right)^2, \tag{1}$$

where $\overline{u}$ is the time-averaged (seasonal mean) zonal wind at longitude $\lambda$ and latitude $\varphi$ and pressure level $p$. The number of elements in the summation, $N$, is equal 90, 91, or 92 days depending on season.

In this section and in the supporting information (SI) we introduce the scale-dependent subseasonal variability integral ($SSVI_k$) as the square root of the vertically and meridionally integrated variance in winds, temperature, and surface pressure fields on terrain-following levels. With the variance integration along the three spatial directions, $SSVI$ denotes the globally integrated subseasonal variability.

### 2.1. Scale-dependent Subseasonal Variability

For the scale-dependent analysis, the circulation is decomposed by horizontal and vertical scales using the normal-mode function (NMF) expansion (Kasahara & Puri, 1981). The NMF decomposition has been extensively applied for the initialization of weather prediction models (Daley, 1991) but also for studies of atmospheric energetics and variability (e.g., Blaauw & Žagar, 2018; Castanheira et al., 2002; Tanaka & Kung, 1988; Žagar et al., 2009). It applies the Hough harmonics for the multivariate representation of the horizontal winds and geopotential height on terrain-following levels after the vertical decomposition. Examples of real-time outputs from the NMF expansion of the deterministic ECMWF forecasts are available at http://modes.fmf.uni-lj.si. The method description is provided in SI and a more detailed presentation can be found in Žagar et al. (2015) and references therein.

The results of the global data expansion in terms of 3-D orthogonal NMFs are time series of the Hough expansion coefficients $\chi_\nu(t) = \chi_n^k(m; t)$ which simultaneously represent wind and geopotential height fields. The latter is a transformed geopotential height variable which consists of hydrostatic geopotential height and a surface pressure term as defined in SI. The three-component index $\nu = (k, n, m)$ of $\chi_\nu$ consists of indices

for the zonal wave number ($k$), the meridional mode index ($n$), and the vertical mode index ($m$). The meridional index $n$ denotes both the Rossby modes (quasi-geostrophic or balanced) and eastward-propagating and westward-propagating inertio-gravity (IG) modes (or unbalanced modes). The large-scale seasonally varying circulation features which project on the IG modes include the Hadley and Walker circulation in the tropics and midlatitude features such as the gradient wind balanced flow within the stratospheric polar vortex and stationary orographic waves due to large-scale orography of Antarctica and Greenland (Žagar et al., 2017). The projection of daily data spanning 35 years results in $\chi_v(t)$ series of independently analyzed time instants. The three-dimensional orthogonality of NMFs provides conditions for statistics in modal space on coefficients $\chi_v(t)$.

The subseasonal variance for a single mode $v$ is denoted $V_v^2$ and it is computed as

$$V_v^2 = \frac{1}{N-1} \sum_{t=1}^{N} g D_m \left( \chi_v(t) - \overline{\chi_v} \right) \left( \chi_v(t) - \overline{\chi_v} \right)^* . \tag{2}$$

Subseasonal variability for a single mode is thus $V_v = V_n^k(m)$. In equation (2) $g$ is gravity and $D_m$ is the equivalent depth, a parameter which couples horizontal motions with vertical modes (details in SI). The conjugate transpose is denoted $*$. The seasonal mean $\overline{\chi_v}$ is computed as $\overline{\chi_v} = 1/N \sum_{t=1}^{N} \chi_v(t)$, with $N$ the number of days per season. The subseasonal variance defined by equation (2) is about twice the value of transient energy defined as the difference between the energy of the time mean component $\overline{\chi_v}$ and the time mean of energy. The proof is in SI. Some properties of the stationary and transient components of the global energy on interannual time scales using the NMF approach were discussed by Tanaka and Kung (1988) and Castanheira et al. (2002).

The vertically and horizontally integrated subseasonal variance defined by equation (2) is equivalent to the globally integrated variance in physical space $S_{dyn}$, after the vertical projection:

$$\sum_k \sum_n \sum_m \left[ V_n^k(m) \right]^2 = \sum_i \sum_j \sum_m S_{dyn}^2(\lambda_i, \varphi_j, m) . \tag{3}$$

Here variance in physical space at point $(\lambda_i, \varphi_j, m)$, $S_{dyn}^2$ is defined as

$$S_{dyn}^2(\lambda_i, \varphi_j, m) = S_m^2(u) + S_m^2(v) + \frac{g}{D_m} S_m^2(h) . \tag{4}$$

The three elements of the summation (4), $S_m^2(u)$, $S_m^2(v)$, and $S_m^2(h)$, denote variances of the wind components and transformed geopotential height variable, respectively, each computed by (1). The summation (4) in physical space with respect to the zonal index $i$ and meridional index $j$ takes place on the horizontal regular Gaussian grid of the $m$th shallow-water layer after the vertical transform. The units of $V_n^k(m)$ and $S_{dyn}(\lambda_i, \varphi_j, m)$ are meters per second. The proof of (3) is provided in SI.

For every analyzed season, we compute the global $SSVI$ as the square root of the globally integrated variance:

$$SSVI = \sqrt{ c_k \sum_{k=0}^{K} \sum_{n=1}^{R} \sum_{m=1}^{M} \left[ V_n^k(m) \right]^2 } , \tag{5}$$

where $c_k = 2$ for $k > 0$ and $c_k = 1$ for $k = 0$ as we present $SSVI$ only for $k > 0$. Within the truncation limits $M$, $R$, and $K$ of the projection, this equation integrates variances in the two horizontal wind components and hydrostatic geopotential height on the selected terrain-following levels and variance in the surface pressure field. With a focus on variability distribution as a function of the zonal wave number, we define the zonal spectrum of subseasonal variability, $SSVI_k$, as

$$SSVI_k = \sqrt{ c_k \sum_{n=1}^{R} \sum_{m=1}^{M} \left[ V_n^k(m) \right]^2 } . \tag{6}$$

The $SSVI$ computation is then $[SSVI]^2 = \sum_{k=0}^{K} [SSVI_k]^2$. Notice that variances in equations (2)–(4) and $SSVI$s in (5)–(6) are time dependent values but we dropped the time index. Notice also that no filtering is performed
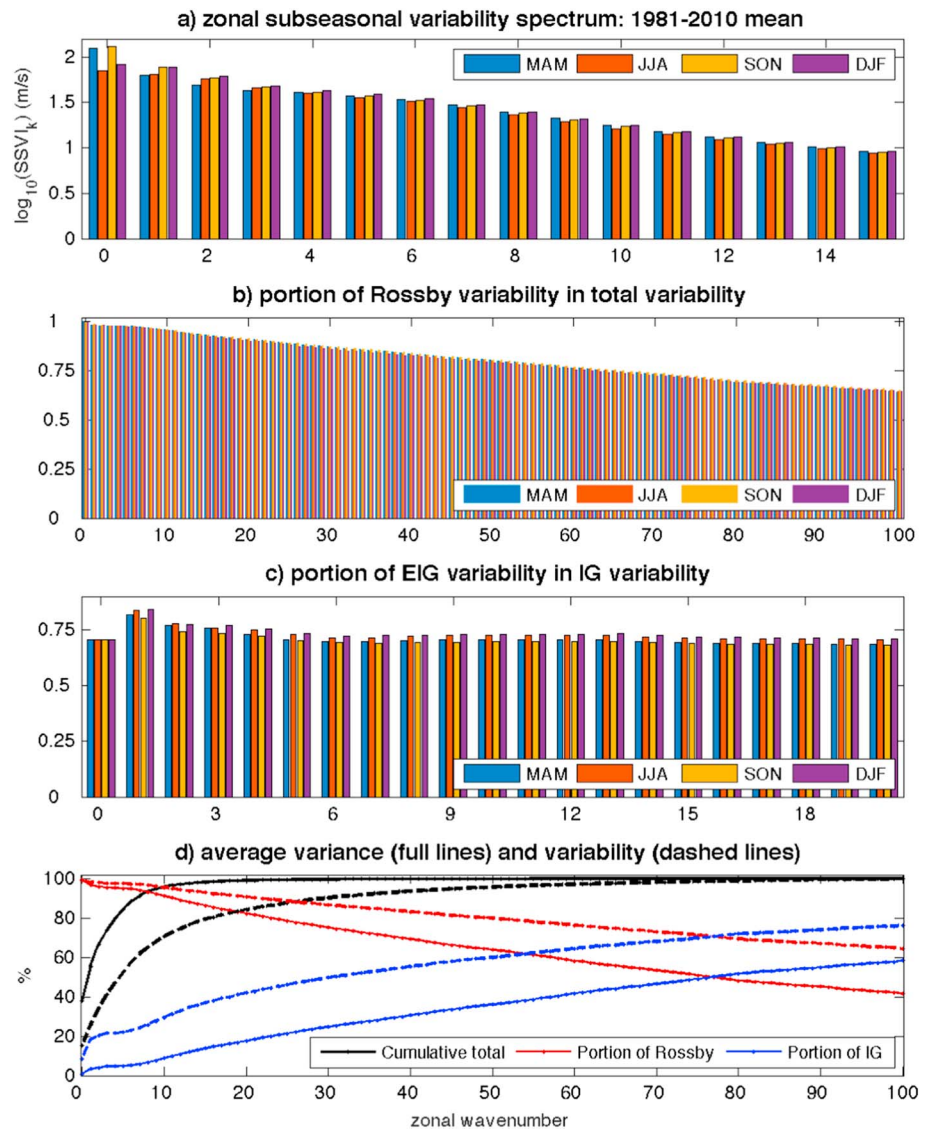
**Figure 1.** Distribution of average subseasonal variability defined by equation (6) in ERA-Interim 43-level data for 1981–2010 period as a function of the zonal wave number. (a) Variability $\overline{SSVI_k}$ in four seasons for zonal wave numbers $k$ = 0–15, (b) portion of variability associated with Rossby modes in each wave numbers, $\overline{SSVI_k}^R/\overline{SSVI_k}$, for $k$ = 0–100, (c) portion of variability associated with the EIG modes in total IG variability in each zonal wave number, $\overline{SSVI_k}^{EIG}/\overline{SSVI_k}^{IG}$, and (d) full lines: cumulative variance in percentages of the total variance in wave numbers $k$ = 0–100 (black line) and percentage of variance in Rossby (red) and IG (blue) modes in each zonal wave number. Dashed lines show the same quantities but for variability. See text for further details. MAM = March-April-May; JJA = June-July-August; SON = September-October-November; DJF = December-January-February; SSVI = subseasonal variability integral; IG = inertio-gravity; EIG = easterly-propagating IG.

on the $\chi_\nu(t)$ time series before the variance computation; that is, $\chi_\nu(t)$ coefficients contain spatiotemporal variability on all scales represented by ERA-Interim data.

Dynamical aspects of subseasonal variability are discussed by separating contributions from the Rossby and IG components. As variances in various modes are additive, for each $k$ we can write $\left[SSVI_k\right]^2 = \left[SSVI_k^R\right]^2 + \left[SSVI_k^{IG}\right]^2$, where the two components denote the subseasonal zonal variance spectra of the Rossby modes and the IG modes, respectively. The associated variability spectra are their square roots, $SSVI_k^R$ and $SSVI_k^{IG}$, respectively. The IG variance can be further separated in variances associated with the eastward- and westward-propagating modes, denoted by EIG and WIG, respectively: $\left[SSVI_k^{IG}\right]^2 = \left[SSVI_k^{EIG}\right]^2 + \left[SSVI_k^{WIG}\right]^2$. The same applies for the global variability integral $SSVI$, $\left[SSVI\right]^2 = \left[SSVI^R\right]^2 + \left[SSVI^{IG}\right]^2$. The mean global variability and variability in
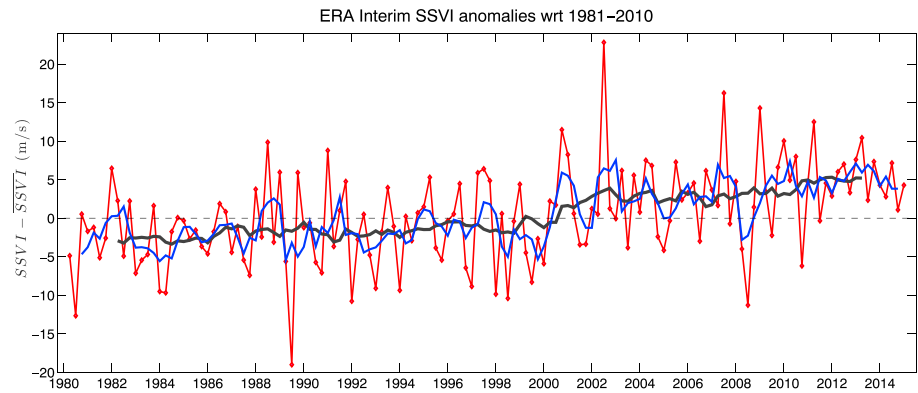
**Figure 2.** Time series of globally integrated subseasonal variability anomalies relative to 1981–2010 in ERA-Interim reanalysis based on 43 levels between the surface and 0.5 hPa. Anomalies for each season are computed with respect to the 30-year seasonal mean. Blue and black curves denote 4-point and 16-point running mean (4 and 16 subsequent seasons), respectively. SSVI = subseasonal variability integral.

wave number $k$ are denoted by $\overline{SSVI}$ and $\overline{SSVI}_k$, respectively, and are computed by averaging the variance over the time period before taking the square root.

### 2.2. Data

The reanalysis data set ERA-Interim is available on 60 hybrid $\sigma - p$ vertical levels once per day at 12 UTC during 35-year period from 1980 to 2014. The reanalysis description is available in Dee et al. (2011) and its basic properties are contrasted to other main reanalyses in Fujiwara et al. (2017). ERA-Interim applies specified sea surface temperatures, sea-ice concentrations, and climatological aerosol fields which have seasonal variations but no longer-term variations of volcanic or other origin. It takes into account increasing level of greenhouse gas concentrations such as $CO_2$ and $CH_4$ (Fujiwara et al., 2017). Low-frequency variability and trends enter reanalysis through the assimilated observations and through variations in sea surface temperature and sea-ice concentration. This information appears to be damped to only a rather small extent by the absence of inter-annual and longer-term changes in radiatively active constituents in the background model (Simmons et al., 2014).

For the NMF projection, winds and hydrostatic geopotential fields were interpolated from the hybrid levels to 43 terrain-following $\sigma$ levels. Their uneven distribution includes 7 levels below 800 hPa, 6 levels between 800 and 500 hPa, 13 levels above 500 hPa up to 100 hPa, 9 levels between 100 and 10 hPa, and the last 8 levels are above 10 hPa up to about 0.5 hPa. The horizontal grid is a regular Gaussian grid including $256 \times 128$ points in the zonal and meridional directions, respectively. By applying the horizontal truncation of $K = 100$ we resolve waves with the horizontal scales down to 200 km at the equator and around 150 km in the midlatitudes. The applied vertical and meridional truncations are $M = 27$ and $R = 150$, respectively; the latter means 50 meridional modes for each among the Rossby, EIG, and WIG waves. The vertical truncation was chosen based on the value of $D_m$ as increasingly smaller equivalent depths implies a stronger trapping of the Hough harmonics near the equator and no improvement in data representation outside the tropics is possible by larger $M$. As discussed by Žagar et al. (2015) and references therein, the applied truncations and the solution method for the NMFs imply that the lower troposphere and high latitudes were not 100% represented by the projection. This does not represent a significant uncertainty since we focus on large scales with most of circulation variability.

The input data once per day provide time series of complex coefficients $\chi_\nu(t)$. Seasonal means $\overline{\chi_\nu}$ are obtained as averages over March-April-May (MAM), June-July-August (JJA), September-October-November (SON), and December-January-February (DJF) seasons. Modal variance $V_\nu^2$ is computed using (2) as the mean square deviation of daily values from seasonal means. The total length of the subseasonal variability time series, which starts with MAM season in 1980, is 139 seasons. A reference 30-year climatology is computed by averaging each season over the period 1981–2010 as in Simmons et al. (2014).
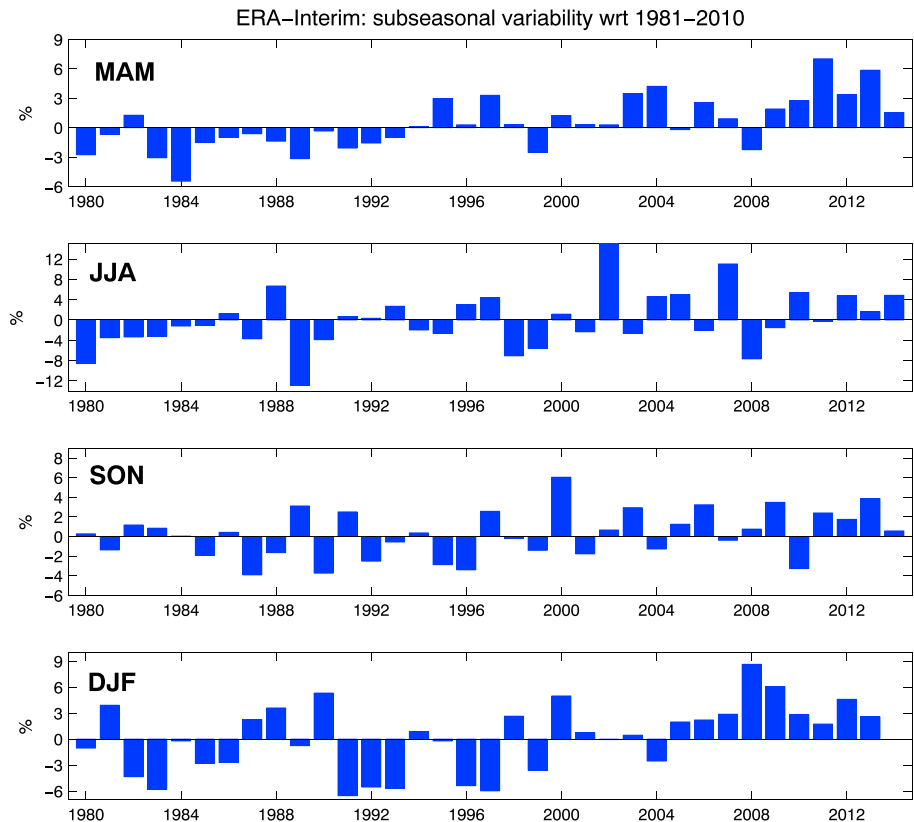
**Figure 3.** Global subseasonal variability anomalies in ERA-Interim reanalyses relative to 1981–2010 mean for each season. Variability is shown in percentages of seasonal mean, $100\% \left( SSVI - \overline{SSVI} \right) / \overline{SSVI}$. MAM = March-April-May; JJA = June-July-August; SON = September-October-November; DJF = December-January-February.

## 3. Results

### 3.1. Spectrum of the Mean Subseasonal Variability

The spectrum of average subseasonal variability $\overline{SSVI}_k$ for the 1981–2010 period is presented in Figure 1 for four seasons. This climatological spectrum encompassing both the troposphere and stratosphere quantifies meridionally and vertically integrated variability as explained in section 2.1. It shows that the subseasonal variability is largest in the zonal mean state ($k = 0$) which also shows a seasonal cycle (Figure 1a). About 15% of the zonally integrated variability is at $k = 0$ ($\overline{SSVI}_{k=0} / \sum_k \overline{SSVI}_k$), which is an average between 18% in MAM and SON and 11–12% in JJA and DJF seasons. This corresponds to around 38% of the subseasonal variance in $k = 0$ (Figure 1d). The seasonal cycle in $k = 0$ is probably related to the polar vortex dynamics on subseasonal time scales.

For $k > 0$, variability decreases with the zonal scale as well as differences between seasons. Among the seasons, DJF has the largest variability in all wave numbers $> 0$. For $k \geq 3$, the difference among seasons is small although JJA systematically appears as the season with the smallest variability. The cumulative $SSVI_k$ curve in Figure 1d shows that around 40% of the globally integrated subseasonal variability is at scales $k = 0$–3 and around 70% at scales $k = 0$–10. Only about 25% of $\overline{SSVI}_k$ resides at smaller scales with $k \geq 14$ (around 1,000 km in the midlatitudes). Although there are no similar spectra to compare with, we stress that the large portion of subseasonal variability at planetary scales is associated with using the data without any prior filtering and a number of levels in the stratosphere.

The majority of subseasonal variability is associated with the balanced large-scale circulation (Figure 1b). At subsynoptic scale $k = 20$, the Rossby part ($\overline{SSVI}_k^R / \overline{SSVI}_k$) stands for almost 90% of variability whereas at the smallest analyzed scales, $k = 100$, the portion is about 64%. The scale where the subseasonal variance associated with the IG modes exceeds variance due to Rossby modes is at $k \approx 75$ (Figure 1d; around 530 km in the tropics and 380 km in midlatitudes). This is not surprising as at this scale divergence-dominated processes projecting on the IG modes prevail over quasi-geostrophic dynamics in nature and in the ECMWF forecast
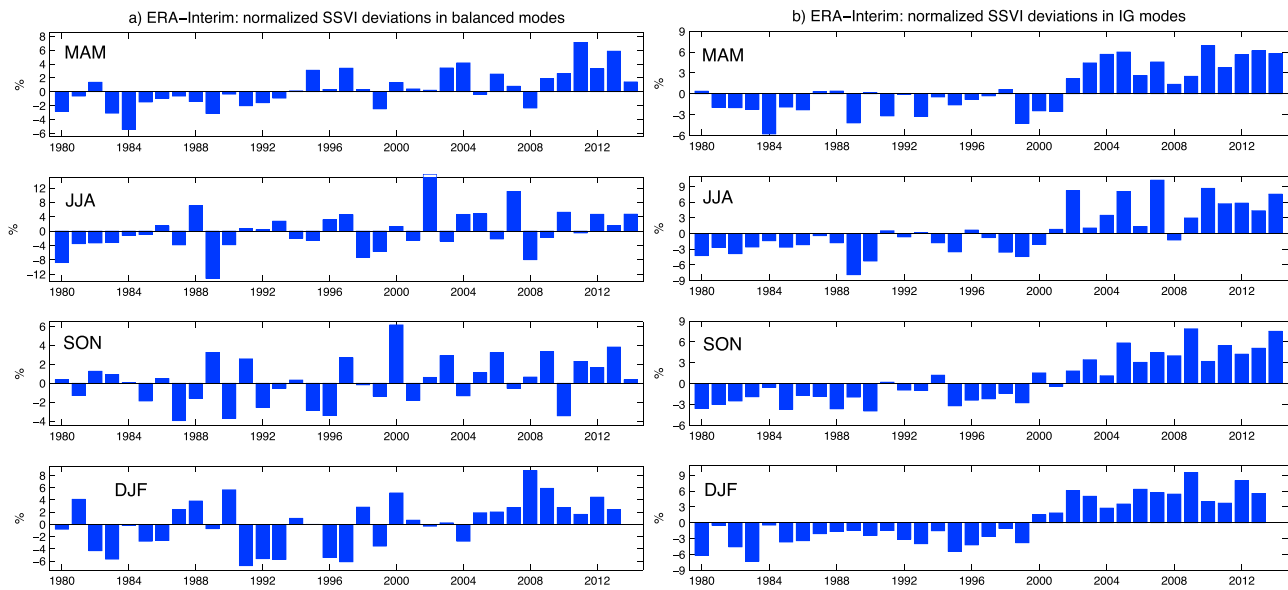
**Figure 4.** As in Figure 3 but for the component of variability projecting on (left) Rossby (balanced) and (right) IG modes. Rossby and IG anomalies are normalized by their respective 1981–2010 means. SSVI = subseasonal variability integral; IG = inertio-gravity; MAM = March-April-May; JJA = June-July-August; SON = September-October-November; DJF = December-January-February.

model used as the basis for the reanalysis (Žagar et al., 2017). This property should nevertheless be considered as mainly produced by the model since at these scales the impact of observations might be significantly smoothed by global data assimilation modeling.

Figure 1c shows that variability associated with the EIG modes significantly exceeds the WIG variability component at all presented scales. The EIG variability level is around 70% across many scales and it exceeds 80% at $k = 1$. However, the WIG variance dominates over EIG on subsynoptic scales (figure not shown) so that in the total sum the EIG-related variance exceeds the WIG part by only a few percent. The prevalence of the EIG-related variance on large scales is most likely related to the role of the tropical Kelvin waves in subseasonal variability, whereas the subsynoptic prevalence of the WIG variance is likely due to IG waves associated with eastward-moving baroclinic waves in the extratropics. The EIG component also shows a seasonal cycle (Figure 1c) which is associated with a strong seasonality in vertically propagating equatorial waves, primarily the Kelvin waves (Blaauw & Žagar, 2018)

These percentages and Figure 1 apply to the selected 43 levels of ERA-Interim and can serve for validation of climate models for the same period provided the model outputs are analyzed on the same grid. The analysis procedure can be performed for different choices of vertical levels leading to different values of the *SSVI* integral. This is illustrated by a figure in SI that is equivalent to Figure 1 except for a different subset of ERA-Interim data (36 levels under 96 hPa). It shows smaller amplitudes of variability but shares all main properties with Figure 1. The differences can be explained by differences in average properties of large-scale circulation in the troposphere and stratosphere. The horizontal grid is not expected to change the *SSVI* much as the majority of the variance is at large scales.

### 3.2. Trends

Figure 2 shows the time series of *SSVI* anomalies computed by equation (5) relative to 1981–2010 period. The anomaly for each season is computed with respect to its respective 30-year mean. Blue and black curves denote annual and 4-year running means, respectively. The total *SSVI* seasonal curves are available as Figure 2 in SI. Normalized anomalies are presented in Figure 3 where each season anomaly relative to its 1981–2010 period mean is normalized by the mean and shown as percentages.

The most interesting characteristic in Figure 2 is a change from mainly negative *SSVI* anomalies before year 2000 and its prevailing positive value ever since. The change is consistent with the increase of precipitation events found by White et al. (2017) and the energy changes reported by Simmons et al. (2017). Figure 3 reveals that largest deviations occurred in boreal summers 1989 and 2002 with amplitudes exceeding 10% of the

mean. They can be further discussed by using the zonal, meridional, and vertical spectra and comparison with model space, in particular the role of stratosphere as there are 17 levels above 100 hPa. The four-season average anomaly has been positive since 2009 (Figure 2) and the last few years are characterized by positive anomalies in all seasons from a few percentage up to about 8% relative to 1981–2010. In the last decade, DJF and MAM appear with more systematic positive anomalies then JJA and SON (Figure 3). The average anomaly since 2009 is about 4 m/s which makes about 2% of the average variability in 1981–2010.

Relative anomalies for the Rossby and IG parts are shown in Figure 4 to study whether the relative changes in the two components have occurred in the same way. Figure 4a, the Rossby (balanced) variability anomalies, is very similar to Figure 3 reflecting the fact that the majority of subseasonal variability is associated with balanced dynamics. For example, the most anomalous season prior 2000, 1989 boreal summer (Figure 3), is found in both the Rossby component and IG component in both 1989 and 1990 (Figure 4). The largest positive anomaly of JJA 2002 is also present in both components. But for a number of seasons the two anomalies do not have the same sign. This reflects the fact that anomalies occurred either in a single or both extratropical belt balanced dynamics or in the tropical latent heating which is the main cause of IG-type variability. The striking difference between anomalies in the two components is on average a larger and systematically positive normalized $SSVI^{IG}$ anomaly than the normalized Rossby variability anomaly, $SSVI^{R}$. Apart from JJA 2008, the IG anomaly is positive since 2001 but it has been on increase since 1999. Although the IG part contributes a smaller component of the global variability, especially on large scales, it is believed to represent a large portion of the tropical variability patterns such as the free-propagating stratospheric Kelvin waves and the Madden-Julian oscillation. Larger relative anomalies in unbalanced circulation and their coupling to the tropics are in agreement with the reported increase in mesoscale convection and precipitation events in the tropics. A supplemental figure showing time series of subseasonal variability anomalies in the Rossby and IG components is in SI (Figure 3).

## 4. Discussion and Conclusions

We applied a modal decomposition for the computation of global $SSVI$ which spatially integrates variability in horizontal wind components and geopotential height, which is modified to include surface pressure, on terrain-following levels. The new variability measure is used for scale quantification of variability in the ERA-Interim reanalyses in recent decades.

The results provide the global spectrum of average subseasonal variability in period 1981–2010 in ERA-Interim. When integrated over 43 levels spanning the troposphere and stratosphere up to 0.5 hPa, the spectrum is characterized by 11% to 18%, depending on season, of variability in the zonal mean state. About 40% of subseasonal variability is in planetary scales with zonal wave numbers 0 to 3, whereas about one-quarter is in subsynoptic scales with zonal wave numbers 15 and greater.

Time series of $SSVI$ anomalies show an increased subseasonal variability after year 2000 with anomalies in recent years at about 2% level above the 1981–2010 average. When variability is separated between two components of dynamics (Rossby and IG), a larger and more persistent increase in the IG component becomes evident. As the integrated IG modes mainly represent tropical circulation patterns, different trends in Rossby and IG parts may reflect reported increase in latent heat in ERA-Interim (Simmons et al., 2017) in relation to the observed increased precipitation variability (White et al., 2017) which is the source of tropical wave motions (e.g., Alexander et al., 2017; Kim & Alexander, 2013).

The subseasonal variability seen in Figures 2–4 can be further separated in symmetric and asymmetric parts, and in the zonal and meridional scales as shown in Figure 1 for the zonal wave numbers. In this way, we can improve our understanding of scales and processes most influenced by climate change. The scale-dependent examination of variability and its trends has a potential for the validation of global climate models using reanalysis data and for the validation of theories proposed to explain recent weather extremes (e.g., Petoukhov et al., 2013).

Our average 2% increase in $SSVI$ in period 2009–2014 relative to 1981–2010 is based on ERA-Interim and not necessarily present in other reanalysis data sets. We focus on the method and its performance for ERA-Interim given the reported trends in precipitation and latent heat in this data set. It can be expected that different reanalyses are less consistent in the tropics than in the midlatitudes due to the lack of direct wind observations in tropical regions and complex dynamics. For example, Harada et al. (2016) showed that the amplitudes

of equatorial waves and Madden-Julian oscillation in JRA-55 reanalyses (Kobayashi et al., 2015) are weaker than in the other reanalyses. Differences between physical parametrizations in the models used to prepare reanalyses largely control the IG spectrum and energy transport across scales (e.g., Malardel & Wedi, 2016). The reanalyses underestimate spatial variability on smaller scales (Žagar et al., 2017) that effects temporal variability. A study of *SSVI* in different reanalyses in the light of their known deficiencies is under way.

## References

Academies National (2016). *Attribution of extreme weather events in the context of climate change*. Washington, DC: The National Academies of Sciences, Engineering, and Medicine Press. https://doi.org/10.17226/21852

Alexander, M. J., Ortland, D. A., Grimsdell, A. W., & Kim, J.-E. (2017). Sensitivity of gravity wave fluxes to interannual variations in tropical convection and zonal wind. *Journal of Atmospheric Science*, *74*, 2701–2716. https://doi.org/10.1175/JAS-D-17-0044.1

Blaauw, M., & Žagar, N. (2018). Multivariate analysis of Kelvin wave seasonal variability in ECMWF L91 analyses. *Atmospheric Chemistry And Physics*, *18*, 8313–8330. https://doi.org/10.5194/acp-18-8313-2018

Castanheira, J. M., Graf, H. F., DaCamara, C., & Rocha, A. (2002). Using a physical reference frame to study global circulation variability. *Journal of Atmospheric Science*, *59*, 1490–1501.

Cubasch, U., Wuebbles, D., Chen, D., Facchini, M. C., Frame, D., Mahowald, N., & Winther, J.-G. (2013). Introduction. In T. F. Stocker, D. Qin, G.-K. Plattner, M. Tignor, S. K. Allen, J. Boschung, et al. (Eds.), *Climate Change 2013: The Physical Science Basis. Contribution of Working Group I to the Fifth Assessment Report of the Intergovernmental Panel on Climate Change* (pp. 119–158). Cambridge, UK and New York: Cambridge University Press. https://doi.org/10.1017/CBO9781107415324.007

Daley, R. (1991). *Atmospheric data analysis* (460 pp.). Cambridge: Cambridge University Press.

Dee, D. P., Uppala, S. M., Simmons, A. J., Berrisford, P., Poli, P., Kobayashi, S., et al. (2011). The ERA-Interim reanalysis: Configuration and performance of the data assimilation system. *Quarterly Journal of the Royal Meteorological Society*, *137*, 553–597.

Fujiwara, M., Wright, J. S., Manney, G. L., Gray, L. J., Anstey, J., Birner, T., et al. (2017). Introduction to the SPARC Reanalysis Intercomparison Project (S-RIP) and overview of the reanalysis systems. *Atmospheric Chemistry and Physics*, *17*, 1417–1452. https://doi.org/10.5194/acp-17-1417-2017

Grise, K. M., & Thompson, D. W. J. (2012). Equatorial planetary waves and their signature in atmospheric variability. *Journal of Atmospheric Science*, *69*, 857–874. https://doi.org/10.1175/JAS-D-11-0123.1

Harada, Y., Kamahori, H., Kobayashi, C., Endo, H., Kobayashi, S., Ota, Y., et al. (2016). The JRA-55 reanalysis: Representation of atmospheric circulation and climate variability. *Journal of the Meteorological Society of Japan*, *94*, 269–302.

Kasahara, A. (1984). The linear response of a stratified global atmosphere to a tropical thermal forcing. *Journal of Atmospheric Science*, *41*, 2217–2237.

Kasahara, A., & Puri, K. (1981). Spectral representation of three-dimensional global data by expansion in normal mode functions. *Monthly Weather Review*, *109*, 37–51.

Kim, J. E, & Alexander, M. J. (2013). Tropical precipitation variability and convectively coupled equatorial waves on submonthly time-scales in reanalyses and TRMM. *Journal Climate*, *26*, 3013–3030.

Knutti, R., & Sedlacek, J. (2013). Robustness and uncertainties in the new CMIP5 climate model projections. *Nature Climate Change*, *3*, 369–373.

Kobayashi, A., Ota, Y., Harada, Y., Ebita, A., Moriya, M., Onoda, H., et al. (2015). The JRA-55 reanalysis: General specifications and basic characteristics. *Journal of the Meteorological Society of Japan*, *93*, 5–48.

Malardel, S., & Wedi, N. P. (2016). How does subgrid-scale parametrisation influence nonlinear spectral energy fluxes in global NWP models? *Journal of Geophysical Research: Atmospheres*, *121*, 5395–5410. https://doi.org/10.1002/2015JD023970

Petoukhov, V., Rahmstorf, S., Petri, S., & Schellnhuber, H. J. (2013). Quasiresonant amplification of planetary waves and recent northern hemisphere weather extremes. *Proceedings of the National Academy of Sciences*, *110*(14), 5336–5341.

Shepherd, T. G. (2014). Atmospheric circulation as a source of uncertainty in climate change projections. *Nature Geoscience*, *7*(703). https://doi.org/10.1038/ngeo2253

Simmons, A. J., Berrisford, P., Dee, D. P., Hersbach, H., Hirahara, S., & Thepaut, J.-N. (2017). A reassessment of temperature variations and trends from global reanalyses and monthly surface climatological datasets. *Quarterly Journal of the Royal Meteorological Society*, *143*, 101–119.

Simmons, A. J., Poli, P., Dee, D. P., Berrisford, P., Hersbach, H., Kobayashi, S., & Peubey, C. (2014). Estimating low-frequency variability and trends in atmospheric temperature using ERA-Interim. *Quarterly Journal of the Royal Meteorological Society*, *140*, 329–353.

Tan, J., Jakob, C., Rossow, W. B., & George, T. (2015). Increases in tropical rainfall driven by changes in frequency of organized deep convection. *Nature*, *519*, 451–454.

Tanaka, H., & Kung, E. (1988). Normal-mode expansion of the general circulation during the FGGE year. *Journal of the Atmospheric Sciences*, *45*, 3723–3736.

White, R. H., Battisti, D. S., & Skok, G. (2017). Tracking precipitation events in time and space in gridded observational data. *Geophysical Research Letters*, *44*, 8637–8646. https://doi.org/10.1002/2017GL074011

Žagar, N., Jelić, D., Blaauw, M., & Bechtold, P. (2017). Energy spectra and inertia-gravity waves in global analyses. *Journal of Atmospheric Science*, *74*, 2447–2466.

Žagar, N., Kasahara, A., Terasaki, K., Tribbia, J., & Tanaka, H. (2015). Normal-mode function representation of global 3-D datasets: Open-access software for the atmospheric research community. *Geoscientific Model Development*, *8*, 1169–1195.

Žagar, N., Tribbia, J., Anderson, J. L., & Raeder, K. (2009). Uncertainties of estimates of inertio-gravity energy in the atmosphere. Part I: Intercomparison of four analysis datasets. *Monthly Weather Reviews*, *137*, 3837–3857. Corrigendum, Mon. Wea. Rev., 138, 2476–2477.